This is a repository copy of *Supramolecular Iron Metallocubanes Exhibiting Site-Selective Thermal and Light-Induced Spin-Crossover*.

White Rose Research Online URL for this paper:
https://eprints.whiterose.ac.uk/153161/

Version: Accepted Version

# Supramolecular Iron Metallocubanes Exhibiting Site-Selective Thermal and Light-Induced Spin-Crossover

Izar Capel Berdiell,[†] Tim Hochdörffer,[¶] Cédric Desplanches,[‡] Rafal Kulmaczewski,[†] Namrah Shahid,[†] Juliusz A. Wolny,[¶] Stuart L. Warriner,[†] Oscar Cespedes,[§] Volker Schünemann,[¶] Guillaume Chastanet*,[‡] and Malcolm A. Halcrow*,[†].

[†]School of Chemistry, University of Leeds, Woodhouse Lane, Leeds LS2 9JT, UK.

[¶]Department of Physics, Technical University of Kaiserslautern, Erwin Schrödinger Str. 46, D-67663 Kaiserslautern, Germany.

[‡]CNRS, Univ. Bordeaux, ICMCB, UMR 5026, F-33600 Pessac, France.

[§]School of Physics and Astronomy, EC Stoner Building, University of Leeds, Leeds LS2 9JT, UK.

**ABSTRACT:** Treatment of $Fe[BF_4]_2 \cdot 6H_2O$ with 4,6-di(pyrazol-1-yl)-1$H$-pyrimid-2-one ($HL^1$) or 4,6-di(4-methylpyrazol-1-yl)-1$H$-pyrimid-2-one ($HL^2$) affords solvated crystals of $[\{Fe^{III}(OH_2)_6\} \subset Fe^{II}_8(\mu\text{-}L)_{12}][BF_4]_7$ (**1**, $HL = HL^1$; **2**, $HL = HL^2$). The centrosymmetric complexes contain a cubic arrangement of iron(II) centers, with *bis*-bidentate $[L]^-$ ligands bridging the edges of the cube. The encapsulated $[Fe(OH_2)_6]^{3+}$ moiety templates the assembly through twelve O−H...O hydrogen bonds to the $[L]^-$ hydroxylate groups. All four unique iron(II) ions in the cages are crystallographically high-spin at 250 K, but undergo a gradual high→low spin-crossover on cooling, which is predominantly centered on one iron(II) site and its symmetry-related congener. This was confirmed by magnetic susceptibility data, LIESST effect measurements and, for **1**, Mössbauer spectroscopy and diffuse reflectance data. The clusters are stable in MeCN solution, and **1** remains high-spin above 240 K in that solvent. The cubane assembly was not obtained from reactions using other iron(II) salts or 4,6-di(pyrazol-1-yl)pyrimidine ligands, highlighting the importance of hydrogen bonding in templating the cubane assembly.

## Introduction

Spin-crossover (SCO) compounds are an important class of molecular switch, which undergo a transition between a high-spin and low-spin electronic configuration under temperature, pressure, irradiation or other physical stimuli.[1-5] This electronic rearrangement also changes the structure of a molecule, and thus of the lattice containing it.[6] As a result, SCO transitions perturb many physical properties of a material.[7] This has been exploited to produce switchable conducting,[8,9] dielectric,[9,10] ferroelectric,[11] fluorescent,[12] mechanically responsive[13] and molecular magnet materials[14] based on SCO components. While SCO is most often observed in molecular crystals and coordination polymers,[15] it can also be incorporated into guest-responsive frameworks[16] and in soft materials.[17] Moreover, SCO switching properties are retained at micro and nano length scales,[4,5,18] and even at the single molecule level.[19] This has led to several applications for SCO compounds in macroscale, nanoscale and molecular devices being demonstrated in prototype form.[4,20]

With this in mind, there is interest in (supra)-molecular assemblies of SCO centers, which can switch between multiple states if their components undergo SCO selectively.[21] Some dinuclear compounds,[21-25] molecular squares[26,27] and grid complexes[28,29] have this property, of undergoing SCO at specific sites under different conditions in the solid state. Tetrahedral coordination cages,[21,22,24,30] metallomacrocycles[31] and a handful of larger assemblies with multiple SCO centers[21,32-38] are also known, although their SCO switching often occurs in a gradual and less well-defined manner. We report here two examples of a supramolecular, templated iron(II) cubane assembly which both undergo SCO at two of their eight vertices. These are the largest molecules yet known to exhibit site-selective SCO.

## Chart 1 The ligands referred to in this work.



R = H, H$L^1$
R = Me, H$L^2$

R = CH$_3$, $L^3$
R = NH$_2$, $L^4$
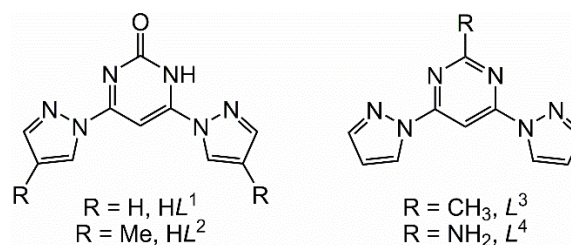
## Experimental Section

2-Methyl-4,6-bis(pyrazol-1-yl)-1,3-pyrimidine ($L^3$),[39] 2-amino-4,6-bis(pyrazol-1-yl)-1,3-pyrimidine ($L^4$)[39] and the reagent sodium 4,6-dichloro-pyrimidin-2-onate[40] were prepared by the literature procedures.

**Synthesis of 4,6-di(pyrazol-1-yl)-1$H$-pyrimid-2-one (H$L^1$).** Sodium 4,6-dichloro-pyrimidin-2-onate (0.59 g, 3.2 mmol), pyrazole (0.50 g, 7.2 mmol) and sodium hydride (0.29 g, 7.2 mmol) were suspended in tetrahydrofuran (40 cm$^3$). The mixture was stirred at 65 °C under N$_2$ for 18 hrs, then the solvent was removed under vacuum affording the sodium salt Na[$L^1$] as a solid residue. This was dissolved in water (35 cm$^3$) and dilute HCl was slowly added until the solution reached $p$H 5. Extracted of the acidified solution with chloroform (3x 50 cm$^3$), followed by evaporation to dryness of the dried washings, afforded H$L^1$ in NMR purity. Yield 0.50 g, 69 %. Mp 223-224 °C. ES$^+$-MS $m/z$ 229.0833 (calcd for $[H_2L^1]^+$ 229.0832), 251.0655 (calcd for $[NaHL^1]^+$ 251.0652). $^1$H NMR ($\langle CD_3 \rangle_2SO$) $\delta$ 6.67 (dd, 1.7 and 2.6 Hz, 2H, Pz $H^4$), 7.82 (s, 1H,

Pym $H^5$), 7.96 (d, 1.7 Hz, 2H, Pz $H^3$), 8.59 (m, 2H, Pz $H^5$). $^{13}$C NMR ($(CD_3)_2SO$) $\delta$ 87.1 (1C, Pym $C^5$), 109.4 (2C, Pz $C^4$), 127.9 (2C, Pz $C^3$), 144.1 (2C, Pz $C^5$), 159.9 (2C, Pym $C^{4/6}$), 164.7 (1C, Pym $C^2$).

**Synthesis of 4,6-di(4-methylpyrazol-1-yl)-1$H$-pyrimid-2-one (H$L^2$).** Method as for H$L^1$, using sodium 4,6-dichloro-pyrimidin-2-onate (0.82 g, 4.4 mmol), 4-methylpyrazole (0.90 g, 10.9 mmol) and sodium hydride (0.5 g, 12.5 mmol) in tetrahydrofuran (50 cm$^3$). The product is a white solid. Yield 0.78 g, 69 %. Mp 228-229 °C. ES$^+$-MS $m/z$ 257.1146 (calcd for [H$_2L^2$]$^+$ 257.1145), 279.0967 (calcd for [NaH$L^2$]$^+$ 279.0965), 301.0785 (calcd for [Na$_2(L^2)$]$^+$ 301.0784), 535.2031 (calcd for [Na(H$L^2$)$_2$]$^+$ 535.2037). $^1$H NMR ($(CD_3)_2SO$) $\delta$ 2.12 (s, 6H, C$H_3$), 7.68 (s, 1H, Pym $H^5$), 7.78 (s, 2H, Pz $H^3$), 8.33 (s, 2H, Pz $H^5$), 12.53 (br s, 1H, N$H$). $^{13}$C NMR ($(CD_3)_2SO$) $\delta$ 8.7 (2C, C$H_3$), 86.1 (1C, Pym $C^5$), 119.4 (2C, Pz $C^4$), 125.9 (2C, Pz $C^3$), 145.1 (2C, Pz $C^5$), 159.7 (2C, Pym $C^{4/6}$), 164.6 (1C, Pym $C^2$).

**Synthesis of [{Fe$^{III}$(OH$_2$)$_6$}⊂Fe$^{II}$$_8$($\mu$-$L^1$)$_{12}$][BF$_4$]$_7$ (1) and [Fe(H$L^1$)$_2$(OH$_2$)$_3$(NCMe)][BF$_4$]$_2$ (4).** A solution of H$L^1$ (0.20 g, 0.88 mmol) in acetonitrile (85 cm$^3$) was added to another solution of Fe[BF$_4$]$_2$·6H$_2$O (0.25 g, 0.73 mmol) in acetonitrile (25 cm$^3$). The mixture was stirred at room temperature for 15 mins, then filtered. Slow diffusion of diethyl ether vapor into the yellow solution, over a period of 3 days, afforded red/orange crystals of **1**·6MeCN with an octahedral morphology, together with an orange powder that was removed by decantation. The crystals are stable to exposure to air at 298 K for a period of hours, but decompose to a solvent-free material after drying *in vacuo*. Yield 0.18 g, 63 %. Elemental analysis for C$_{120}$H$_{96}$B$_7$F$_{28}$Fe$_9$N$_{72}$O$_{18}$ found (calcd) (%) C, 36.7 (36.5), H, 2.22 (2.45), N, 25.4 (25.6). ESMS $m/z$ 570.7 (13, [Fe(H$_2$O)$_6$⊂Fe$_8(L^1)_{12}$(BF$_4$)]$^{6+}$), 702.3 (57, [Fe(H$_2$O)$_6$⊂Fe$_8(L^1)_{12}$(BF$_4$)$_2$]$^{5+}$), 899.3 (80, [Fe(H$_2$O)$_6$⊂Fe$_8(L^1)_{12}$(BF$_4$)$_3$]$^{4+}$), 1228.1 (100, [Fe(H$_2$O)$_6$⊂Fe$_8(L^1)_{12}$(BF$_4$)$_4$]$^{3+}$), 1885.6 (7, [Fe(H$_2$O)$_6$⊂Fe$_8(L^1)_{12}$(BF$_4$)$_5$]$^{2+}$). $^1$H NMR (CD$_3$CN) $\delta$ 5.9, 60.1 (both 24H, Pz $H^3$ and $H^5$), 79.7 (24H, Pz $H^4$), 114.1 (12H, Pym $H^5$).

On one occasion, a paler yellow crystal of [Fe(H$L^1$)$_2$(OH$_2$)$_3$(NCMe)][ClO$_4$]$_2$ (**4**) was isolated from one of these crystallization vials, and crystallographically characterized. This compound could not be isolated in pure form, however, so its analytical characterization was not achieved.

**Synthesis of [{Fe$^{III}$(OH$_2$)$_6$}⊂Fe$^{II}$$_8$($\mu$-$L^2$)$_{12}$][BF$_4$]$_7$ (2).** A solution of H$L^2$ (0.050 g, 0.20 mmol) in acetonitrile (7.5 cm$^3$) was added to another solution of Fe[BF$_4$]$_2$·6H$_2$O (0.026 g, 0.078 mmol) in acetonitrile (5 cm$^3$). The mixture was stirred at 298 K for 2 hrs, then filtered. Slow diffusion of a mixture of diethyl ether and di-isopropyl ether into the yellow solution, over a period of 3-5 days, afforded red crystals of **2**·$x$MeCN·$y$Et$_2$O. These crystals decompose readily on exposure to air to a solvent-free powder. Yield 0.029 g, 79 %. Elemental analysis for C$_{144}$H$_{144}$B$_7$F$_{28}$Fe$_9$N$_{72}$O$_{18}$ found (calcd) (%) C, 40.2 (40.4), H, 3.46 (3.39), N, 23.4 (23.6). ESMS $m/z$ 983.4 (11, [Fe(H$_2$O)$_6$⊂Fe$_8(L^2)_{12}$(BF$_4$)$_3$]$^{4+}$), 1340.2 (100, [Fe(H$_2$O)$_6$⊂Fe$_8(L^2)_{12}$(BF$_4$)$_4$]$^{3+}$), 2053.8 (50, [Fe(H$_2$O)$_6$⊂Fe$_8(L^2)_{12}$(BF$_4$)$_5$]$^{2+}$). Other fragmentation peaks of <20 % intensity are not assigned. $^1$H NMR (CD$_3$CN) $\delta$ 4.8, 60.4 (both 24H, Pz $H^3$ and $H^5$), 9.5 (36H, C$H_3$), 112.7 (12H, Pym $H^5$).

**Synthesis of [Fe(H$L^1$)$_2$(OH$_2$)$_2$(NCMe)$_2$][ClO$_4$]$_2$ (3).** Filtered solutions of H$L^1$ (20 mg, 0.088 mmol) in acetonitrile (3 cm$^3$) was mixed with Fe[ClO$_4$]$_2$·6H$_2$O (31 mg, 0.088 mmol) in acetonitrile (4 cm$^3$), affording an intensely yellow solution. The solution was stirred at room temperature for 2 hrs, then left to slowly evaporate under ambient conditions. Orange crystals of **3** appeared on the wall of the vial after 2 days, together with a larger quantity of an amorphous material of unknown composition. Yield 19 mg, 35 %.

Elemental analysis for C$_{14}$H$_{18}$Cl$_2$FeN$_8$O$_{11}$ found (calcd) (%) C, 27.8 (28.0); H, 2.85 (3.02), N, 18.4 (18.6).

**CAUTION. Although we have experienced no issues while handling 3, metal-organic perchlorates are potentially explosive and should be handled with care in small quantities.**

**Synthesis of *catena*-[Fe($\mu$-$L^3$)(OH$_2$)(solv)][BF$_4$]$_2$ (5, solv = acetone; 5b, solv = H$_2$O).** Filtered solutions of $L^3$ (22 mg, 0.097 mmol) in acetone (7 cm$^3$), and of Fe[BF$_4$]$_2$·6H$_2$O (30 mg, 0.089 mmol) in acetone (5 cm$^3$), were mixed to afford a yellow solution that slowly deposited a small amount of insoluble yellow powder upon standing. After the precipitation ceased the solution was filtered, and the supernatant was crystallized by slow diffusion of diethyl ether vapor. One such reaction afforded yellow single crystals of formula [Fe($L^3$)(OH$_2$)(acetone)][BF$_4$]$_2$·H$_2$O (**5**·H$_2$O, see below). However, on other occasions this procedure yielded an insoluble yellow powder analysing as [Fe($L^3$)(OH$_2$)$_2$][BF$_4$]$_2$ (**5b**), where the coordinated acetone is presumably replaced by another water ligand. Yield 21 mg, 43 % yield. Elemental analysis for C$_{11}$H$_{14}$B$_2$F$_8$FeN$_6$O$_2$ (**5b**) found (calcd) (%) C, 26.7 (26.9), H, 2.78 (2.87), N, 17.0 (17.1).

### Single Crystal Structure Analyses

Diffraction data for H$L^1$ and **1**·6CH$_3$CN were recorded at station I19 of the Diamond synchrotron ($\lambda$ = 0.6889 Å). Other crystallographic data were measured with an Agilent Supernova dual-source diffractometer using monochromated Cu-$K_\alpha$ ($\lambda$ = 1.5418 Å) radiation. All the structures were solved by direct methods (*SHELXS97*[41]), and developed by full least-squares refinement on $F^2$ (*SHELXL97*[41]). Experimental details for the structure determinations (Tables S1-S3) and descriptions of the crystallographic refinements are given in the Supporting Information.

Crystallographic figures were prepared using *XSEED*.[42] Octahedral coordination volumes ($V_{Oh}$) and the volumes of the metal-lacubane cages were calculated with *Olex2*.[43] Bond valence sum calculations were performed using literature parameters for high-spin and low-spin Fe−N and Fe−O bonds.[44]

### Other measurements

Crystals of **1**·6MeCN and **2**·$x$MeCN·$y$Et$_2$O were sent to collaborating labs for Mössbauer spectroscopy, LIESST and diffuse reflectance measurements. Since loss of lattice solvent from those materials could occur during transit or sample preparation, the solvent content of the samples used for those measurements is uncertain. Dried, polycrystalline **1** and **2** have reduced long-range order but otherwise retain their solid state structures, from X-ray powder diffraction and magnetic susceptibility data (Figures S13-S15).

Elemental microanalyses were performed by the London Metropolitan University microanalytical service. Electrospray mass spectra were recorded on a Bruker MicroTOF-q instrument, from CHCl$_3$ solution (organic compounds) or CH$_3$CN solution (metal complexes). Diamagnetic NMR spectra employed a Bruker DPX300 spectrometer operating at 300.1 MHz ($^1$H) or 75.5 MHz ($^{13}$C), while paramagnetic NMR spectra used a Bruker Ascend400 (400.1 MHz) or Jeol JNM-ECA600II (600.1 MHz) spectrometer. X-ray powder diffraction data were measured using a Bruker D2 Phaser diffractometer. Simulated powder patterns were produced by *Lazy Pulverix*,[45] which is part of the *XSeed* software suite.[42]

Solid state magnetic susceptibility measurements were performed on a Quantum Design MPMS-3 magnetometer, with an applied field of 5000 G and a scan rate of 5 Kmin$^{-1}$. Freshly prepared **1**·6MeCN and **2**·$x$MeCN·$y$Et$_2$O were protected from solvent loss during the measurements with a drop of diethyl ether in the sealed sample holder. Diamagnetic corrections for the sample (estimated from Pascal's constants)[46] and the sample holder were

applied to the data. Magnetic measurements in solution were obtained by Evans method using a Bruker Avance500 spectrometer operating at 500.13 MHz.[47] A diamagnetic correction for the sample,[47] and a correction for the variation of the density of the solvent with temperature,[48] were applied to these data.

Diffuse reflectance data were obtained using a home-built reflectivity set-up coupled to a CVI spectrometer, which allows us to collect both the reflectivity spectra in the 450-950 nm range at a given temperature and to follow the temperature dependence of the signal at a selected wavelength (± 2.5 nm) between 5-290K. The instrument is equipped with an optical detector, which collects the whole reflected intensity affording the total reflectivity signal as a function of temperature. The white light source is a halogen lamp emitting between 300-2400 nm. This analysis was directly performed on thin layer of the available solid samples in form of polycrystalline powder without any dispersion in a matrix.

Photomagnetic measurements were performed using a set of photodiodes coupled *via* an optical fibre to the cavity of a MPMS-55 Quantum Design SQUID magnetometer operating at 20 kOe. The powder sample was prepared in a thin layer (~0.1 mg on around 100 $\mu$m thickness) to promote full penetration of the irradiated light. The sample mass was obtained by comparison with the thermal spin transition curve measured on a larger, accurately weighed polycrystalline sample. The sample was first slow cooled to 10 K, ensuring that potential trapping of HS species at low temperatures did not occur. Irradiation was carried out at 405, 510, 650, 830 and 1550 nm. The power of the sample surface was adjusted to 5 mW cm$^{-2}$ (calibrated outside the SQUID magnetometer). Irradiation at 650 nm was found to be most efficient in this system. Once photo-saturation was reached, irradiation was ceased and the temperature increased at a rate of 0.3 K min$^{-1}$ to ~100 K and the magnetization measured every 1 K to determine the $T$(LIESST) value given by the minimum of the $\delta\chi_M T/\delta T$ *vs* $T$ curve for the relaxation.[49] The magnetization was also measured in the absence of irradiation between 10−290 K, to follow the thermal spin transition and to obtain a low temperature baseline.

$^{57}$Fe Mössbauer spectra were obtained in transmission geometry using a constant acceleration spectrometer operated in conjunction with a 512-channel analyser in the time-scale mode (WissEl GmbH). The source contained $^{57}$Co diffused in Rh with an activity of 1.4 GBq. The spectrometer was calibrated against α-iron at room temperature. A continuous flow cryostat (OptistatDN, Oxford Instruments) was utilized for variable temperature measurements. Spectra were simulated using the public domain program *Vinda* running in Excel 2003®.[50] The spectra were analysed by least-squares fits using Lorentzian line shapes. In addition to the Mössbauer isomer shift $\delta$ and quadrupole splitting $\Delta E_Q$ parameters, the linewidth at half maximum $\Gamma$ is given in Table S14.

## Results and Discussion

The new ligands 4,6-di(pyrazol-1-yl)-1H-pyrimid-2-one (H$L^1$) and 4,6-di(4-methylpyrazol-1-yl)-1H-pyrimid-2-one (H$L^2$, Chart 1) were prepared in 69 % yield, by reaction of sodium 4.6-dichloro-2-pyrimidonate[40] with 2.25 equiv of the appropriate pyrazole in the presence of sodium hydride as base. Crystallographic data show both ligands adopt the 4,6-di(pyrazol-1-yl)-1*H*-pyrimid-2-one tautomeric structure shown in Chart 1, rather than the alternative 2-hydroxy-4,6-di(pyrazol-1-yl)pyrimidine form (Figures S3 and S4). This is also evident by $^{13}$C NMR in ⟨CD$_3$⟩$_2$SO solution, where the pyrimidone *C*2 atoms resonate at 164.6-164.7 ppm, as expected for a carbonyl C atom.

Treatment of Fe[BF$_4$]$_2$·6H$_2$O with 1.2 equiv H$L^1$ or H$L^2$ in MeCN affords bright yellow solutions, which deposit [⟨Fe(OH$_2$)$_6$⟩⊂Fe$_8$($\mu$-$L^1$)$_{12}$][BF$_4$]$_7$·6MeCN (**1**·6MeCN) or [⟨Fe(OH$_2$)$_6$⟩⊂Fe$_8$($\mu$-$L^2$)$_{12}$][BF$_4$]$_7$·$x$MeCN·$y$Et$_2$O (**2**·$x$MeCN·$y$Et$_2$O)

as red/orange prisms upon slow diffusion of diethyl ether antisolvent. Yields of these syntheses were variable, at 30-65 % for **1** and up to 79 % for **2**. Fresh crystals of **2**·$x$MeCN·$y$Et$_2$O have $x = y =$ 2.5, but this solvent content was slowly lost during multiple data collections from the same crystal (Table S2). That solvent loss had no effect on the quality of the diffraction data over the timescale of the experiment, although drying the crystals *in vacuo* leads to loss of long-range order.

The assemblies comprise a [Fe$_8$($\mu$-$L$)$_{12}$]$^{4+}$ ([$L$]$^-$ = [$L^1$]$^-$ or [$L^2$]$^-$) cluster with a cubane connectivity, encapsulating a [Fe(OH$_2$)$_6$]$^{3+}$ guest molecule that spans a crystallographic inversion center (Figure 1). The assignment of the cubane vertices as iron(II) centers, and the encapsulated guest as an iron(III) species was supported by bond valence sum calculations (Tables S12 and S13),[51] and by Mössbauer spectroscopy of **1** as described below.
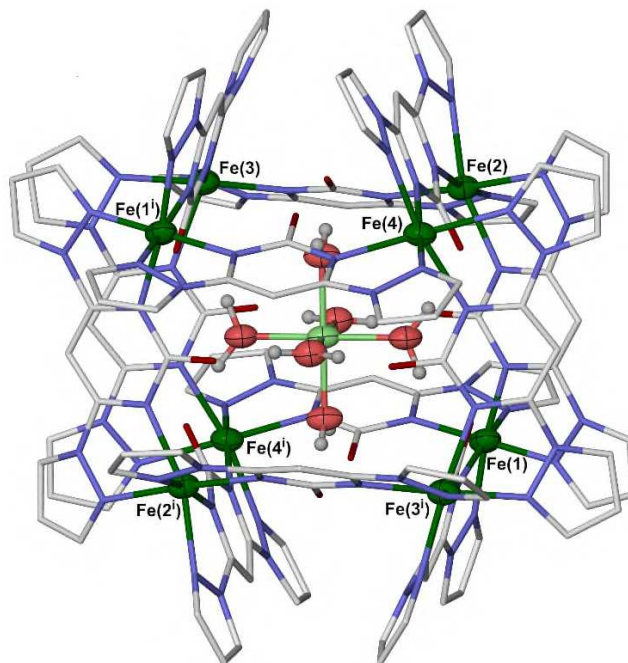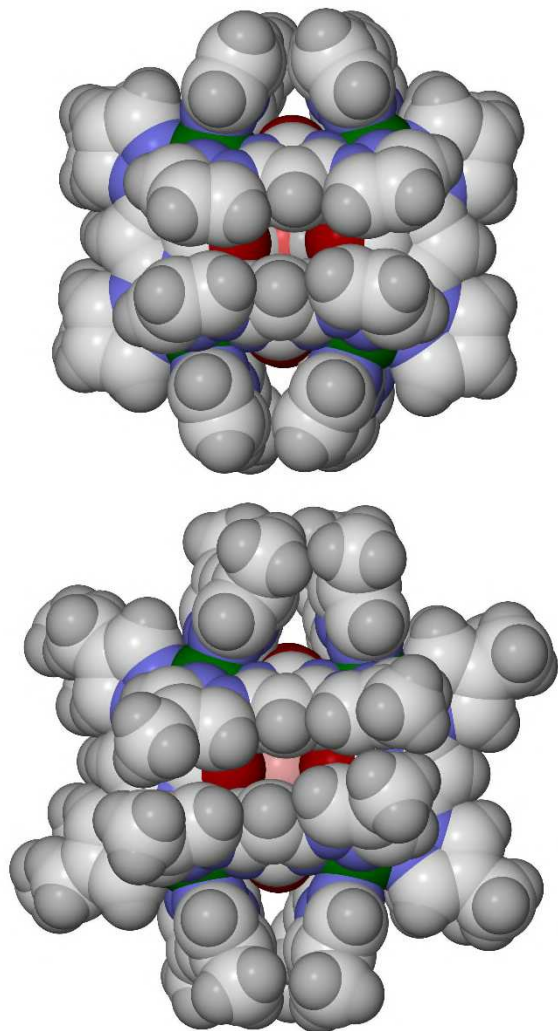


**Figure 1.** The [⟨Fe(OH$_2$)$_6$⟩⊂Fe$_8$($\mu$-$L^1$)$_{12}$]$^{7+}$ assembly in **1**·6MeCN at 100 K Only one orientation of the disordered pyrazolyl groups is shown, and C-bound H atoms have been omitted. The encapsulated [Fe(OH$_2$)$_6$]$^{3+}$ cation, centered on Fe(5), is shown with pale coloration. Color code: C, white; H, pale grey; Fe, green; N, blue; O, red. Symmetry code (i) 3/2–*x*, 1/2–*y*, 1−*z*.

Each [$L$]$^-$ ligand bridges two iron atoms along the edges of the cube in *bis*-bidentate fashion, yielding *fac*-[Fe($L$)$_3$]$^{2+}$ vertices with alternating $\Lambda$ and $\Delta$chirality. The Fe...Fe distances along the edges of the cubane in **1** are 6.216(3)-6.351(3) Å at 100 K, and its internal volume is *ca* 90 Å$^3$.[52] The aqua ligands of the guest cation are oriented to the centers of the faces of the cubane, and each donates short hydrogen bonds to the O atoms from two [$L^1$]$^-$ ligands [O⟨OH$_2$⟩...O⟨$L^1$⟩ = 2.588(4)-2.614(4) Å at 100 K].[53] The corresponding parameters in **2** are essentially the same as for **1**, although its Fe...Fe distances span a slightly narrower range (Tables S7-S11). The assemblies differ, however, in the conformations of their [$L$]$^-$ ligands which are noticably more twisted in **2** than in **1**. That may be caused by steric contacts between the [$L^2$]$^-$ methyl substituents, on ligands on opposite edges of each face of the cubane (Figure 2). These methyl groups are separated by C...C = 3.5-3.7 Å, which is within the sum of their Pauling Van der Waals radii (4.0 Å$^{54}$).

Further consideration of **1**·6MeCN is complicated by pyrazolyl group disorder, reflecting intramolecular steric clashes between $[L^1]^-$ ligands (Figure S9). However, insight is provided by the volume of the FeN$_6$ or FeO$_6$ coordination octahedra ($V_{Oh}$), which is a common crystallographic measure of spin states in SCO complexes (Table 1). High- and low-spin iron(II) complexes with bidentate diimine ligands typically exhibit $V_{Oh} \approx 13$ and 10 Å$^3$, respectively.[55] By that measure, Fe(1) in **1**·6MeCN exhibits gradual SCO on cooling. The high-temperature onset of this SCO is *ca* 300 K, by extrapolation of the data, while the transition is 80 ± 5 % complete at 100 K. While the other unique vertices Fe(2)-Fe(4) are high-spin at 250 K, Fe(2) also shows the onset of gradual SCO below 150 K. Vertices Fe(3) and Fe(4), and the $[Fe(OH_2)_6]^{3+}$ guest Fe(5), remain fully high-spin at all the temperatures investigated.

No such ligand disorder occurs in **2**·*x*MeCN·*y*Et$_2$O, which affords a clearer picture of the spin states in that molecule. In this case, $V_{Oh}$ indicates that all four unique iron(II) centers in the asymmetric unit are high-spin at 250 K (Table 2). Cooling the crystals induces gradual SCO in Fe(1) below 250 K, while small reductions in $V_{Oh}$ for Fe(2) and Fe(3) in the 125 K structure also imply the onset of SCO at those centers. Atoms Fe(4) and Fe(5) in **2**·*x*MeCN·*y*Et$_2$O remain fully high-spin on cooling, as before. Hence, SCO in both compounds occurs predominantly at Fe(1) and its symmetry equivalent in the centrosymmetric cluster, with the onset of SCO at one or two other cubane vertices also being evident at the low-temperature limits of the measurements.

Apart from the bond length changes at Fe(1), SCO has little effect on the dimensions of the $[Fe_8(\mu\text{-}L)_{12}]^{4+}$ cages. However, some pyrazolyl groups bound to Fe(1) and Fe(3) in **1** are displaced by up to 0.50 Å between the high-spin and low-spin structures (Figure S11). This may allow the SCO-induced contraction at Fe(1) and Fe(1$^i$) to occur without significantly changing the internal volume of the cages, which is constrained by the $[Fe(OH_2)_6]^{3+}$ guest.[52] Smaller heavy atom displacements of ≤0.35 Å occur in **2** on cooling, possibly because the SCO at Fe(1) is less complete at 125 K in that compound (Figure S12). The steric influence of the encapsulated $[Fe(OH_2)_6]^{3+}$ might explain the incompleteness of SCO in **1** and **2**, by inhibiting contraction of the cages that would result upon SCO at the other vertices.



**Figure 2.** Space-filling views of the $[\langle Fe(OH_2)_6\rangle \subset Fe_8(\mu\text{-}L)_{12}]^{7+}$ clusters in **1**·6MeCN at 100 K (top), and **2**·*x*MeCN·*y*Et$_2$O at 125 K (bottom), showing the more twisted ligand conformations in the latter compound. Both views look down a OH$_2$−Fe−OH$_2$ axis in the $[Fe(OH_2)_6]^{3+}$ guest. Other details as for Figure 1.

**Table 2** Volumes of the coordination octahedra ($V_{Oh}$, Å$^3$)[55] about each unique iron atom in the crystal structures of **2**·*x*MeCN·*y*Et$_2$O (Figure S8). Full metric parameters for this compound are in Table S6.

| $T$ (K) | 125 | 200 | 250 |
|---|---|---|---|
| $V_{Oh}\langle Fe(1)\rangle$ | 11.359(11) | 12.704(11) | 12.935(13) |
| $V_{Oh}\langle Fe(2)\rangle$ | 12.507(12) | 12.801(10) | 12.876(13) |
| $V_{Oh}\langle Fe(3)\rangle$ | 12.686(12) | 12.819(10) | 12.826(13) |
| $V_{Oh}\langle Fe(4)\rangle$ | 12.906(12) | 12.910(10) | 12.915(13) |
| $V_{Oh}\langle Fe(5)\rangle$ | 10.589(8) | 10.635(7) | 10.604(9) |

**Table 1** Volumes of the coordination octahedra ($V_{Oh}$, Å$^3$)[55] about each unique iron atom in the crystal structures of **1**·6MeCN (Figures 1 and S7). Average values are given for Fe atoms coordinated by disordered pyrazolyl groups, with the range of values shown by all possible combinations of these disorder sites in parentheses. Full metric parameters for this compound are in Table S5.

| $T$ (K) | 100 | 150 | 200 | 250 |
|---|---|---|---|---|
| $V_{Oh}\langle Fe(1)\rangle$ | 10.67(3) [10.26(2)–11.06(2)] | 10.88(6) [10.45(3)–11.32(3)] | 11.58(6) [11.07(3)–12.09(3)] | 12.27(6) [11.79(3)–12.74(3)] |
| $V_{Oh}\langle Fe(2)\rangle$ | 12.39(3) [12.33(2)–12.45(2)] | 12.61(3) [12.59(2)–12.62(2)] | 12.76(3) [12.71(2)–12.80(2)] | 12.77(3) [12.77(2)–12.77(2)] |
| $V_{Oh}\langle Fe(3)\rangle$ | 12.93(4) [12.53(2)–13.33(2)] | 13.04(6) [12.70(3)–13.38(3)] | 12.93(6) [12.56(3)–13.30(3)] | 12.78(6) [12.30(3)–13.25(3)] |
| $V_{Oh}\langle Fe(4)\rangle$ | 12.824(12) | 12.759(16) | 12.815(15) | 12.852(16) |
| $V_{Oh}\langle Fe(5)\rangle$ | 10.635(9) | 10.754(12) | 10.742(11) | 10.756(12) |

The higher temperature SCO at Fe(1) in **2** may have a geometric origin, according to the dihedral angles between the three bidentate ligand fragments coordinated to each vertex. These angles should be 90° in an ideal *tris*-chelate complex, where all ligands are perpendicular to each other. However, the average inter-ligand dihedral angle in high-spin **2**·$x$MeCN·$y$Et$_2$O at 250 K is 84.95(12)° for Fe(1), 79.57(12)° for Fe(2), 75.46(10)° for Fe(3) and 71.17(10)° for Fe(4) (Table S8). Hence, the arrangement of $[L^2]^-$ ligands about Fe(2)-Fe(4) is significantly more twisted than for Fe(1). This is also reflected in the $\Sigma$ bond angle parameter, which shows that more twisted ligand geometries induce greater deviations from an ideal octahedral coordination geometry at each vertex (Table S8).[56] Thus, the more geometrically flexible high-spin state should be stabilized in Fe(2)-Fe(4), disfavoring SCO at those sites as observed.[6] $\Sigma$ for Fe(1) decreases at 125 K, reflecting its spin transition,[55] but otherwise these parameters vary only slightly on cooling. That is consistent with the small structural changes during SCO noted above.
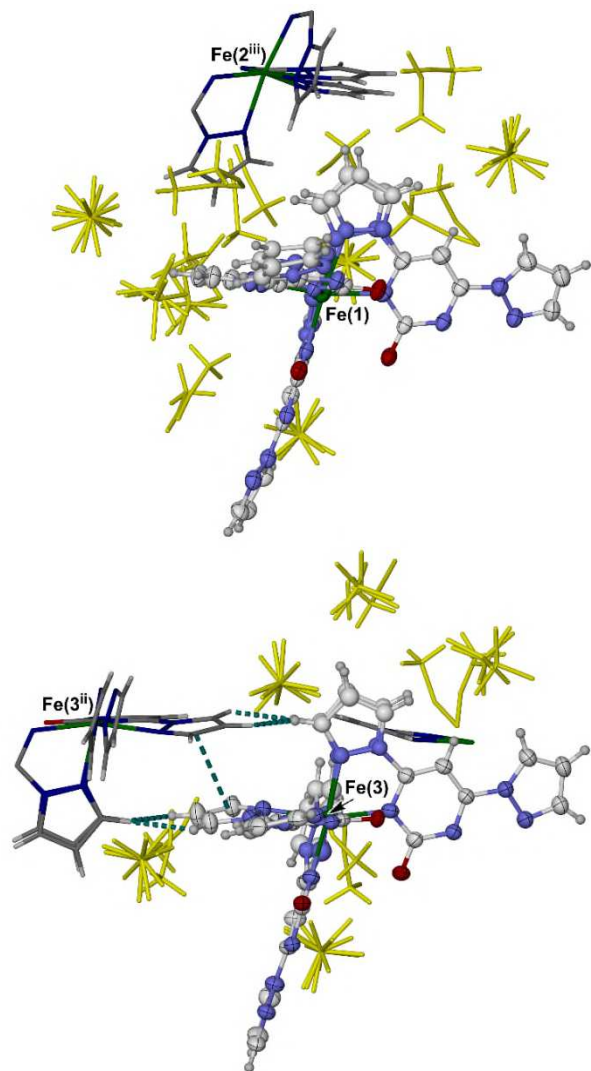


**Figure 3** The lattice environments about the $[Fe(L^1)_3]^-$ fragments centered on Fe(1) and Fe(3) in **1**·6MeCN at 250 K. The main residues have 30 % displacement ellipsoids, while neighbor molecules are de-emphasized. Short contacts between ligands bound to Fe(3) and Fe(3$^{ii}$), which might inhibit SCO at that vertex, are highlighted. Color code: C, white or dark grey; H, pale grey; Fe, green; N, pale or dark blue; O, red; BF$_4^-$ or MeCN, yellow. Symmetry codes: (ii) 1−$x$, 1−$y$, 1−$z$; (iii) $^3/_2$−$x$, −$^1/_2$+$y$, $^3/_2$−$z$.

While a similar analysis for **1**·6MeCN is again impeded by its ligand disorder, Fe(1) and Fe(3) have apparently less distorted geometries than Fe(2) and Fe(4) in that cubane assembly at 250 K. That would disfavor SCO at Fe(2) and Fe(4) in **1**·6MeCN, as above. Moreover, the lattice cavity occupied by the ligands bound to SCO-active Fe(1) is more open and disordered than for Fe(3), one of whose ligands forms a close steric contact with its symmetry equivalent bound to Fe(3$^{ii}$) (symmetry code: (ii) 1−$x$, 1−$y$, 1−$z$; Figure 3). Its more constricted environment could prevent Fe(3) undergoing the geometric changes that would accompany SCO.[6] This combination of geometric and intermolecular steric factors might explain why SCO occurs preferentially at Fe(1) in that compound. There are no obvious packing effects to influence SCO in **2**·$x$MeCN·$y$Et$_2$O, where each cubane vertex forms a comparable distribution of intermolecular contacts.

Magnetic susceptibility data were obtained from freshly prepared polycrystalline **1**·6MeCN and **2**·$x$MeCN·$y$Et$_2$O, which were protected during the measurements to minimize solvent loss. Both compounds yielded $\chi_M T$ = 32 cm$^3$mol$^{-1}$K at 300 K, consistent with an assembly of eight high-spin iron(II) [$\chi_M T \approx 3.5$ cm$^3$mol$^{-1}$K] and one high-spin iron(III) [4.2 cm$^3$mol$^{-1}$K] center (Figure 4). $\chi_M T$ for both compounds gradually decreases on cooling, to a shallow plateau of 22-24 cm$^3$mol$^{-1}$K between 50-100 K. However the variation in $\chi_M T$ between 300-50 K is less monotonic for **2** than for **1**, implying **2** undergoes SCO less gradually than **1** and with a lower onset temperature. The plateau $\chi_M T$ values are slightly lower than expected for SCO occurring at Fe(1) only [*ca* 25 cm$^3$mol$^{-1}$K], indicating partial SCO at other cubane vertices may occur at lower temperatures. These aspects are all consistent with the crystallographic data (Tables 1 and 2). For both compounds, $\chi_M T$ decreases increasingly rapidly below 50 K, which mostly reflects zero-field splitting of the remaining high-spin centers at these temperatures.[57-59] The midpoint temperature $T_{\frac{1}{2}}$ for the higher temperature SCO from these data is similar for both compounds, at *ca* 175 K for **1**·6MeCN and 170 K for **2**·$x$MeCN·$y$Et$_2$O (Figure 4).
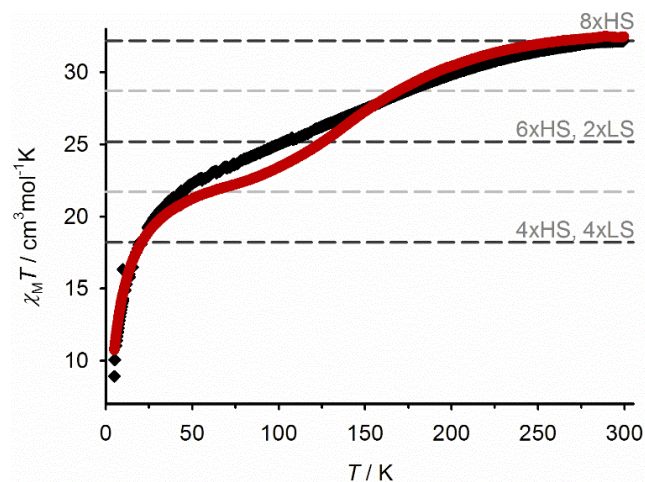


**Figure 4** Solid state magnetic susceptibilty data for **1**·6MeCN (black) and **2**·$x$MeCN·$y$Et$_2$O (red). The dark dashed lines show estimated $\chi_M T$ values for different spin state populations of the iron(II) cubane vertices, while the pale gray lines indicate the midpoints of each stepwise SCO.

SCO in **2** is well defined by the crystallographic and magnetic data. However, the behavior of **1** is less clear-cut because of its more gradual nature, and because the crystallographic disorder in **1**·6MeCN complicates determination of the spin state of Fe(1)-Fe(4) by that technique (Figure 5). To address that ambiguity, SCO in **1** was investigated further by other methods. Since the

samples lost solvent while in transit to collaborator laboratories, the following data were obtained from solvent-free samples of **1**. Importantly, solvent-free **1** and **2** retain their local structure integrity by X-ray powder diffraction (Figure S13). Magnetic data from dried **1** and **2** also closely resemble their solvated crystals, although the $\chi_M T$ *vs* $T$ curve for **1** has a less defined low-temperature plateau than for **1**·6MeCN (Figures S14 and S15).
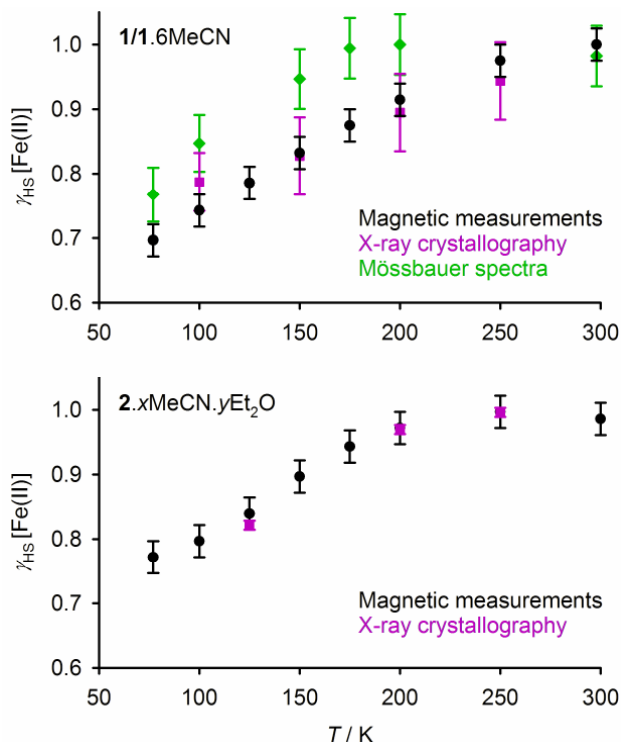


**Figure 5** The high-spin iron(II) fraction ($\gamma_{HS}$) in the cubane vertices of **1** and **2**, as monitored by different measurement techniques (Table S15).

[57]Fe Mössbauer spectra of **1** are shown in Figures 6 and S16. At 77 K the spectrum shows a strong asymmetry which decreases with increasing temperature. This cannot be explained by the presence of texture in the powder sample, since texture effects are temperature independent. Therefore, the Mössbauer spectra were analysed with three main components (Figure 6, Table 3). First is a singlet with an isomer shift $\delta = 0.55$ mms$^{-1}$ at 77 K characteristic for a high spin iron(III) species. Since these parameters are very close to those reported for the ferric hexaquo complex in frozen solution ($\delta = 0.50$ mms$^{-1}$, $\Delta E_Q = 0$),[60] this singlet is due to the $[Fe(OH_2)_6]^{3+}$ cation encapsulated within a cubic local environment. Secondly, a doublet with $\delta = 1.15$ mms$^{-1}$ and $\Delta E_Q = 1.65$ mms$^{-1}$ represents high-spin iron(II) sites[61] at the corners of the $[Fe_8(\mu\text{-}L^1)_{12}]^{4+}$ cub ane. Lastly a doublet with $\delta = 0.42$ mms$^{-1}$ and $\Delta E_Q = 0.55$ mms$^{-1}$, which is not present at $T \geq 175$ K, is assigned to low-spin iron(II). In addition, a minor *ca.* 3 % high-spin Fe(II) impurity is also present in the spectra, whose identity is discussed below. Notably our analyses of the 295, 200 and 175 K Mössbauer spectra each show separate high-spin iron(II) and iron(III) environments in a 1:8 ratio (Table 3, Figure S16) which underlines the assignments described above.

The relative contribution of the low-spin iron(II) doublet increases below $T \leq 150$ K, reaching a *ca* 1:3 ratio of low-spin:high-spin iron(II) atoms at 77 K. That implies SCO has occurred at around one-quarter of the iron(II) sites at that temperature, which is in qualitative agreement with the crystallographic and magnetic data from **1**. However, SCO in the Mössbauer spectra evidently

occurs at lower temperature than by the other techniques, with $T_{1/2}$ shifted to 130±20 K (Figure 5). This may reflect desolvation of the sample before measurement, as mentioned above. No significant line broadening of the high-spin iron(II) doublet occurs below 175 K, showing the local symmetry of the cluster is preserved at all temperatures. That may imply that each vertex undergoes SCO simultaneously with its symmetry equivalent in the centrosymmetric cubane assembly.
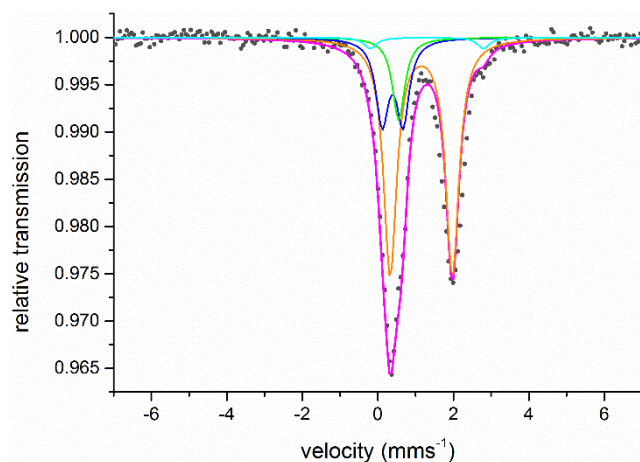


**Figure 6** The Mössbauer spectrum of **1** at 77 K. The simulation is in pink, with its components color coded as: high-spin iron(II) (orange); low-spin iron(II) (blue); high-spin iron(III) (green); and iron(II) impurity (cyan). Spectra at other temperatures are shown in Figure S16.

**Table 3 Relative populations of the iron sites in the Mössbauer spectra of 1 (HS = high-spin, LS = low-spin). The spectra and simulations used to derive these parameters are shown in Figure S16 and Table S14.**

| $T$ (K) | HS Fe(II) | LS Fe(II) | HS Fe(III) | Fe(II) Impurity |
|---|---|---|---|---|
| 298 | 82.8 ±2.0 | 0 | 10.4 ± 2.0 | 6.9 ±3.0 |
| 200 | 84.3 ±2.0 | 0 | 10.5 ±2.0 | 5.2 ±2.0 |
| 175 | 83.8 ±2.0 | 0 | 10.5 ±2.0 | 5.8 ±2.0 |
| 150 | 79.8 ±2.0 | 6.8 ±2.0 | 10.0 ±2.0 | 3.4 ±1.0 |
| 100 | 71.4 ±2.0 | 15.6 ±2.0 | 10.2 ±2.0 | 2.9 ±1.0 |
| 77 | 64.7 ±2.0 | 21.6 ±2.0 | 10.8 ±2.0 | 2.9 ±1.0 |

The presence of low-spin iron(II) in **1** and **2** at low temperature was confirmed by the observation of light-induced excited spin state trapping (LIESST), upon irradiation of the solid compounds at 650 nm at 10 K (Figures 7 and S17).[62,63] Low→high spin photoconversions of *ca* 35 % for **1** and 65 % for **2** were achieved under these conditions, as estimated from the maximum $\chi_M T$ values shown by the irradiated samples before the onset of LIESST relaxation.[64] Despite their different photoconversions, the thermal relaxation of the metastable high-spin centers in the two compounds occurs at essentially the same temperature, with $T$(LIESST) = 67 K for **1** and 68 K for **2**. This agrees well with the predicted value of $T$(LIESST) = 69 K when $T_{1/2}$ = 170 K, according to the previously proposed empirical relationship eq 1 [$T_0$ = 120 K for iron(II) complexes of bidentate ligands].[63,65]

$$T(\text{LIESST}) = T_0 - 0.3\,T_{1/2} \tag{1}$$
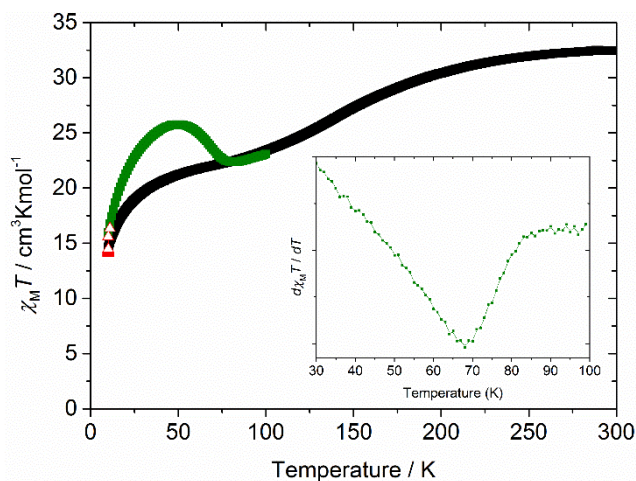
**Figure 7** Magnetic susceptibility data for **2** upon cooling in the dark (black); irradiation at 650 nm at 10 K (red); and then re-warming (green). The inset shows the derivative of the data from the irradiated sample, whose minimum corresponds to $T$(LIESST).

Diffuse reflectance spectra of **1** were measured at five temperatures (Figure S18). While the spectra show a vibronic temperature-dependence that is independent of SCO, there is a clear increase in absorbance between 550-750 nm at 150 and 120 K. This is characteristic for MLCT transitions of low-spin iron(II) complexes with N-heterocyclic ligands,[66] and indicates the occurrence of SCO in the sample. This absorbance decreases again at 70 and 10 K reflecting excitation of the low-spin iron sites by the incident white light, which become trapped in their high-spin excited state below $T$(LIESST).[62]

A more comprehensive temperature dependence of the UV/vis spectrum was recorded using total reflectivity measurements, which show two clear discontinuities (Figure S19). An additional drop in reflectance on cooling below 170 K is close to the onset of SCO in dried **1** by Mössbauer spectroscopy (Figure 5), which converts some iron(II) centers to their more absorbing low-spin form as above.[66] The increase in reflectance around 65 K reflects excitation by the white incident light of the low-spin fraction of the sample, which becomes trapped in its high-spin excited state at

temperatures below $T$(LIESST). The data below 60 K imply the sample has returned to a fully high-spin state (Figure S19), which contrasts with the lower LIESST photoconversion achieved in the SQUID magnetometer (Figure S17). Be that as it may, these data confirm the thermal and light-induced spin state changes observed in **1**.

The $^1$H NMR spectra of **1** and **2** in CD$_3$CN exhibit a single contact-shifted, $C_2$-symmetric [$L$]$^-$ ligand environment (Figures S20 and S21). Electrospray mass spectra of **1** from MeCN solution show a clean progression of peaks corresponding to [{Fe(OH$_2$)$_6$}⊂Fe$_8$($L^1$)$_{12}$(BF$_4$)$_n$]$^{(7-n)+}$ molecular ions with $1 \leq n \leq 5$ (Figures 8, S22 and S23). The mass spectrum of **2** shows more fragmentation than **1**, but includes [{Fe(OH$_2$)$_6$}⊂Fe$_8$($L^2$)$_{12}$(BF$_4$)$_m$]$^{(7-m)+}$ ($m$ = 4 and 5) as its strongest peaks (Figure S24). Both data imply that the [{Fe(OH$_2$)$_6$}⊂Fe$_8$($\mu$-$L$)$_{12}$]$^{7+}$ assemblies retain their integrity in this solvent. Magnetic susceptibility data from **1** in CD$_3$CN showed a constant $\chi_M T = 31.4 \pm 0.4$ cm$^3$mol$^{-1}$K between 237-343 K (Figure S25). Hence the cluster remains fully high spin over the liquid range of that solvent, which is consistent with its solid state behavior.

Analogous complexations of H$L^1$ using Fe[ClO$_4$]$_2$·6H$_2$O or Fe[CF$_3$SO$_3$]$_2$ yielded yellow complex products, without the darker coloration characteristic of **1** and **2**. Mononuclear [Fe(H$L^1$)(OH$_2$)$_2$(NCMe)$_2$][ClO$_4$]$_2$ (**3**) was often obtained from such solutions, containing a protonated H$L^1$ ligand (Figure S26). Hence, the cubane assembly in **1** was only obtained in the presence of the BF$_4^-$ counterion. Closely related [Fe(H$L^1$)(OH$_2$)$_3$(NCMe)][BF$_4$]$_2$ (**4**) was also obtained on one occasion, as a byproduct in the synthesis of **1** (Figures S27 and S28). Hence [Fe(H$L$)(OH$_2$)$_z$(NCMe)$_{4-z}$]$^{2+}$ species may be intermediates in the synthesis of **1** and **2**, which could be initiated by deprotonation of metal-bound H$L^1$ or H$L^2$ by adventitious F$^-$ produced by hydrolysis of BF$_4^-$ in the reaction medium.[67] Compound **4** could also be the minor paramagnetic impurity detected in the Mössbauer spectroscopy study of **1**.

Complexation of Fe[BF$_4$]$_2$·6H$_2$O by $L^3$ or $L^4$ [39] yielded pale yellow powders, one of which afforded the 1D coordination polymer [Fe($\mu$-$L^3$)(OH$_2$)(OCMe$_2$)][BF$_4$]$_2$·H$_2$O (**5·H$_2$O**) after recrystallization from acetone/diethyl ether (Figures S29 and S30). All these results highlight the importance of O–H...O hydrogen bonding in templating the cubane cluster.
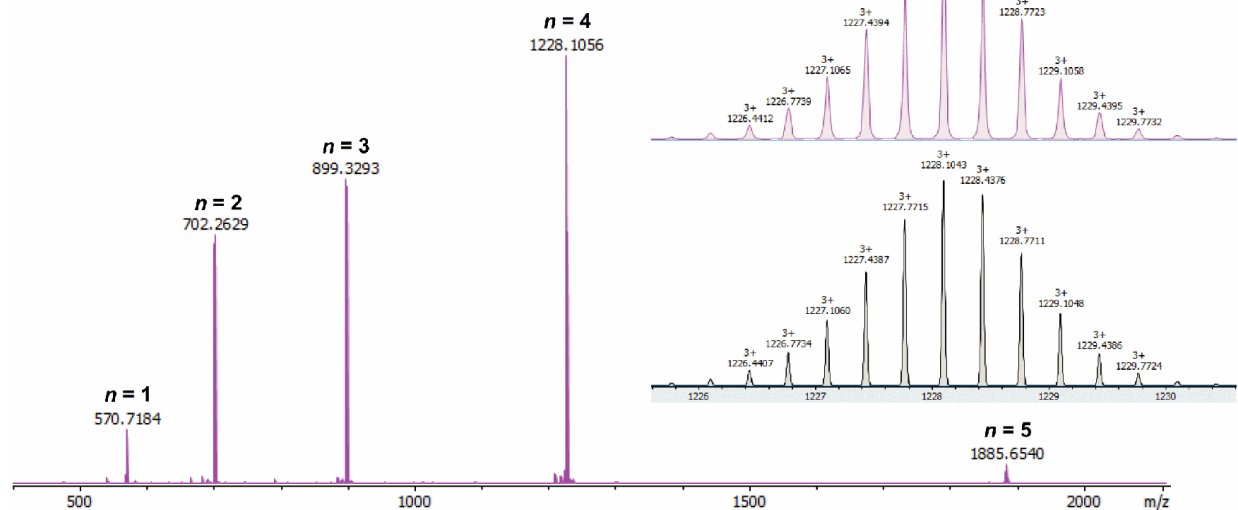


**Figure 8** Electrospray mass spectrum of **1**, showing the [{Fe(OH$_2$)$_6$}⊂Fe$_8$($\mu$-$L^1$)$_{12}$(BF$_4$)$_n$]$^{(7-n)+}$ peak progression. The inset shows an expansion (top) and simulation (bottom) of the principal $n$ = 4 peak. Simulations of the other peaks are in Figure S23.

## Conclusions

The [⟨Fe(OH$_2$)$_6$⟩⊂Fe$_8$($\mu$-$L$)$_{12}$]$^{7+}$ (H$L$ = H$L^1$ or H$L^2$, Chart 1) motif in **1** and **2** is one of the largest SCO-active supramolecular assemblies.[21,32-38] Unusually, both compounds undergo SCO at specific positions among their chemically equivalent metal sites.[37] SCO in **1**·6MeCN is gradual and difficult to quantify because of crystallographic disorder, and because SCO is apparently shifted to *ca* 50 K lower temperature in the desolvated samples used for some measurements. However SCO in **2**·*x*MeCN·*y*Et$_2$O, which lacks this disorder, is well-defined. In both freshly-prepared compounds, SCO at higher temperatures occurs at two symmetry-related iron(II) vertices with $T_{\frac{1}{2}}$ = 170-175 K from crystallographic and magnetic data. Onset of gradual SCO at some other vertices is also apparent in the lowest temperature crystal structure of each compound. LIESST measurements confirm the presence of a low-spin Fe(II) fraction in **1** and **2** at low temperatures which, for **1**, was further quantified with Mössbauer and diffuse reflectance spectra.

SCO at Fe(1) and Fe(1$^i$) has little effect on the volume of the [Fe$_8$($\mu$-$L$)$_{12}$]$^{4+}$ cages (Figure 1).[52] Hence the incomplete SCO shown by **1** and **2** might be explained by the steric influence of the [Fe(OH$_2$)$_6$]$^{3+}$ guest, which would inhibit contraction of the cage upon SCO at the other vertices. The specific observation of SCO at the Fe(1) site in **2** can be attributed to its coordination geometry, which is closer to ideal $C_3$ symmetry than the other vertices in that cubane. Although such details in **1** are masked by its structural disorder, coordination geometry and intermolecular packing influences were identified that might explain the site-selective SCO in that compound.

Formation of **1** and **2** requires hydrogen-bonding templation between the encapsulated [Fe(OH$_2$)$_6$]$^{3+}$ and deprotonated [$L$]$^-$, which may also contribute to their persistence in solution. Our current work aims to investigate the generality of this self-assembly process, and the use of different guest species to tune the SCO properties of the cage.

## ASSOCIATED CONTENT

The Supporting Information is available free of charge on the ACS Publications website at DOI: 10.1021/####.
Full experimental procedures and analytical characterization for the new compounds; crystallographic Figures and Tables for the ligand and complex structures; Mössbauer spectra and simulated parameters; and additional solid and solution phase characterization data.

**Accession Codes**

CCDC-1861171−1861177 and 1938349−1938353 contain the supplementary crystallographic data for this paper. These data can be obtained free of charge via www.ccdc.cam.ac.uk/data_request/cif, or by emailing data_request@ccdc.cam.ac.uk, or by contacting The Cambridge Crystallographic Data Center, 12 Union Road, Cambridge CB2 1EZ, UK; fax: +44 1223 336033.

## AUTHOR INFORMATION

### Corresponding Author

*E-mail: guillaume.chastanet@icmcb.cnrs.fr (G. C.)
*E-mail: m.a.halcrow@leeds.ac.uk (M. A. H.)

### Author Contributions

All authors have given approval to the final version of the manuscript.

## ACKNOWLEDGMENT

## Notes

The authors declare no competing financial interest.

## REFERENCES

(1) Gütlich, P.; Goodwin, H. A. (eds.) *Spin Crossover in Transition Metal Compounds I-III, Topics in Current Chemistry*; Springer-Verlag: Berlin, 2004; Vols. 233−235.

(2) Halcrow, M. A. (ed), *Spin-Crossover Materials - Properties and Applications,* John Wiley & Sons, Ltd.: New York, 2013, p. 568.

(3) Zarembowitch, J.; Varret, F.; Hauser, A.; Real, J. A.; Boukheddaden, K. Spin Crossover Phenomenon − Preface and Introduction *C. R. Chimie* **2018**, *21*, 1056−1059.

(4) Kumar, K. S.; Ruben, M. Emerging Trends in Spin Crossover (SCO) Based Functional Materials and Devices. *Coord. Chem. Rev.* **2017**, *346*, 176−205.

(5) Molnár, G.; Rat, S.; Salmon, L.; Nicolazzi, W.; Bousseksou, A. Spin Crossover Nanomaterials: From Fundamental Concepts to Devices. *Adv. Mater.* **2018**, *30*, 17003862/1−23.

(6) Halcrow, M. A. Structure:Function Relationships in Molecular Spin-Crossover Complexes. *Chem. Soc. Rev.* **2011**, *40*, 4119-4142.

(7) Kahn, O.; Kröber, J.; Jay, C. Spin Transition Molecular Materials for Displays and Data Recording. *Adv. Mater.* **1992**, *4*, 718−728.

(8) See *eg* (a) Takahashi, K.; Cui, H.-B.; Okano, Y.; Kobayashi, H.; Mori, H.; Tajima, H.; Einaga, Y; Sato, O. Evidence of the Chemical Uniaxial Strain Effect on Electrical Conductivity in the Spin-Crossover Conducting Molecular System: [Fe$^{III}$(qnal)$_2$][Pd(dmit)$_2$]$_5$·acetone. *J. Am. Chem. Soc.* **2008**, *130*, 6688−6689. (b) Rotaru, A.; Gural'skiy, I. A.; Molnár, G.; Salmon, L.; Demont, P.; Bousseksou, A. Spin State Dependence of Electrical Conductivity of Spin Crossover Materials. *Chem. Commun.* **2012**, *48*, 4163−4165. (c) Phan, H.; Benjamin, S. M.; Steven, E.; Brooks, J. S.; Shatruk, M. Photomagnetic Response in Highly Conductive Iron(II) Spin-Crossover Complexes with TCNQ Radicals. *Angew. Chem. Int. Ed.* **2015**, *54*, 823−827. (d) Zhang, X.; Wang, Z.-X.; Xie, H.; Li, M.-X.; Woods, T. J.; Dunbar, K. R. A Cobalt(II) Spin-Crossover Compound with Partially Charged TCNQ Radicals and an Anomalous Conducting Behavior. *Chem. Sci.* **2016**, *7*, 1569−1574. (e) Wang, H.-Y.; Ge, J.-Y.; Hua, C.; Jiao, C.-Q.; Wu, Y.; Leong, C. F.; D'Alessandro, D. M.; Liu, T.; Zuo, J.-L. Photo- and Electronically Switchable Spin-Crossover Iron(II) Metal-Organic Frameworks Based on a Tetrathiafulvalene Ligand. *Angew. Chem. Int. Ed.* **2017**, *56*, 5465−5470.

(9) Diaconu, A.; Lupu, S.-L.; Rusu, I.; Risca, I.-M.; Salmon, L.; Molnár, G.; Bousseksou, A.; Demont, P.; Rotaru, A. Piezoresistive Effect in the [Fe(Htrz)$_2$(trz)](BF$_4$) Spin Crossover Complex. *J. Phys. Chem. Lett.* **2017**, *8*, 3147−3151.

(10) See *eg* (a) Nakano, M.; Matsubayashi, G.; Matsuo, T. Dielectric Behavior of Manganese(III) Spin-Crossover Complex [Mn(taa)].*Phys. Rev. B.* **2002**, *66*, 212412/1-4. (b) Bonhommeau, S.; Guillon, T.; Daku, L. M. L.; Demont, P.; Costa, J. S.; Létard, J.-F.; Molnár, G.; Bousseksou, A. Photoswitching of the Dielectric Constant of the Spin-Crossover Complex [Fe(L)(CN)$_2$]·H$_2$O. *Angew. Chem. Int. Ed.* **2006**, *45*, 1625−1629. (c) Zheng, H.; Meng, Y.-S.; Zhou, G.-L; Duan, C.-Y.; Sato, O.; Hayami, S.; Luo, Y.; Liu, T. Simultaneous Modulation of Magnetic and Dielectric Transition via Spin-Crossover-Tuned Spin Arrangement and Charge Distribution. *Angew. Chem. Int. Ed.* **2018**, *57*, 8468−8472. (d) Rat, S.; Piedrahita-Bello, M.; Salmon, L.; Molnár, G.; Demont, P.; Bousseksou, A. Coupling Mechanical and Electrical Properties in Spin Crossover Polymer Composites. *Adv. Mater.* **2018**, *30*, 1705275/1−6.

(11) (a) Jornet-Mollá, V.; Duan, Y.; Giménez-Saiz, C.; Tang, Y.-Y.; Li, P.-F.; Romero, F. M.; Xiong, R.-G. A Ferroelectric Iron(II) Spin Crossover Material. *Angew. Chem. Int. Ed.* **2017**, *56*, 14052–14056. (b) Han, W.-K.; Qin, L.-F.; Pang, C.-Y.; Cheng, C.-K.; Zhu, W.; Li, Z.-H.; Li, Z.; Ren, X.; Gu, Z.-G. Polymorphism of a Chiral Iron(II) Complex: Spin Crossover and Ferroelectric Properties. *Dalton Trans.* **2017**, *46*, 8004–8008.

(12) See *eg* (a) Garcia, Y.; Robert, F.; Naik, A. D.; Zhou, G.; Tinant, B.; Robeyns, K.; Michotte, S.; Piraux, L. Spin Transition Charted in a Fluorophore-Tagged Thermochromic Dinuclear Iron(II) Complex. *J. Am. Chem. Soc.* **2011**, *133*, 15850–15853. (b) Wang, C.-F.; Li, R.-F.; Chen, X.-Y.; Wei, R.-J.; Zheng, L.-S.; Tao, J. Synergetic Spin Crossover and Fluorescence in One-Dimensional Hybrid Complexes. *Angew. Chem. Int. Ed.* **2015**, *54*, 1574–1577. (c) Herrera, J. M.; Titos-Padilla, S.; Pope, S. J. A.; Berlanga, I.; Zamora, F.; Delgado, J. J.; Kamenev, K. V.; Wang, X.; Prescimone, A.; Brechin, E. K.; Colacio, E. Studies on Bifunctional Fe(II)-Triazole Spin Crossover Nanoparticles: Time-Dependent Luminescence, Surface Grafting and the Effect of a Silica Shell and Hydrostatic Pressure on the Magnetic Properties. *J. Mater. Chem. C* **2015**, *3*, 7819–7829. (d) Lochenie, C.; Schötz, K.; Panzer, F.; Kurz, H.; Maier, B.; Puchtler, F.; Agarwal, S.; Köhler, A.; Weber, B. Spin-Crossover Iron(II) Coordination Polymer with Fluorescent Properties: Correlation between Emission Properties and Spin State. *J. Am. Chem. Soc.* **2018**, *140*, 700–709. (e) Wang, J.-L.; Liu, Q.; Meng, Y.-S.; Liu, X.; Zheng, H.; Shi, Q.; Duan, C.-Y.; Liu, T. Fluorescence Modulation via Photoinduced Spin Crossover Switched Energy Transfer from Fluorophores to Fe$^{II}$ Ions. *Chem. Sci.* **2018**, *9*, 2892–2897. (f) Yuan, J.; Wu, S.-Q.; Liu, M.-J.; Sato, O.; Kou, H.-Z. Rhodamine 6G-Labeled Pyridyl Aroylhydrazone Fe(II) Complex Exhibiting Synergetic Spin Crossover and Fluorescence. *J. Am. Chem. Soc.* **2018**, *140*, 9426–9433.

(13) See *eg* (a) Shepherd, H. J.; Gural'skiy, I. A.; Quintero, C. M.; Tricard, S.; Salmon, L.; Molnár, G.; Bousseksou, A. Molecular Actuators Driven by Cooperative Spin-State Switching. *Nature Commun.* **2013**, *4*, 2607/1-9. (b) Vicente, A. I.; Joseph, A.; Ferreira, L. P.; de Deus Carvalho, M.; Rodrigues, V. H. N.; Duttine, M.; Diogo, H. P.; Minas da Piedade, M. E.; Calhorda, M. J.; Martinho, P. N. Dynamic Spin Interchange in a Tridentate Fe(III) Schiff-Base Compound. *Chem. Sci.* **2016**, *7*, 4251–4258. (c) Manrique-Juarez, M. D.; Mathieu, F.; Shalabaeva, V.; Cacheux, J.; Rat, S.; Nicu, L.; Leïchlé, T.; Salmon, L.; Molnár, G.; Bousseksou, A. A Bistable Microelectromechanical System Actuated by Spin-Crossover Molecules. *Angew. Chem. Int. Ed.* **2017**, *56*, 8074–8078.

(14) See *eg* (a) Ohkoshi, S.; Imoto, K.; Tsunobuchi, Y.; Takano, S.; Tokoro, H. Light-Induced Spin-Crossover Magnet. *Nature Chem.* **2011**, *3*, 564-569. (b) Ababei, R.; Pichon, C.; Roubeau, O.; Li, Y.-G.; Bréfuel, N.; Buisson, L.; Guionneau, P.; Mathonière, C.; Clérac, R. Rational Design of a Photomagnetic Chain: Bridging Single-Molecule Magnets with a Spin-Crossover Complex. *J. Am. Chem. Soc.* **2013**, *135*, 14840–14853. (c) Feng, X.; Mathonière, C.; Jeon, I.-R.; Rouzières, M.; Ozarowski, A.; Aubrey, M. L.; Gonzalez, M. I.; Clérac, R.; Long, J. R. Tristability in a Light-Actuated Single-Molecule Magnet. *J. Am. Chem. Soc.* **2013**, *135*, 15880–15884. (d) Mathonière, C.; Lin, H.-J.; Siretanu, D.; Clérac, R.; Smith, J. M. Photoinduced Single-Molecule Magnet Properties in a Four-Coordinate Iron(II) Spin Crossover Complex. *J. Am. Chem. Soc.* **2013**, *135*, 19083–19086. (e) Urtizberea, A.; Roubeau, O. Switchable Slow Relaxation of Magnetization in the Native Low Temperature Phase of a Cooperative Spin-Crossover Compound. *Chem. Sci.* **2017**, *8*, 2290–2295. (f) Shao, D.; Shi, L.; Yin, L.; Wang, B.-L.; Wang, Z.-X.; Zhang, Y.-Q.; Wang, X.-Y. Reversible On-Off Switching of Both Spin Crossover and Single-Molecule Magnet Behaviours via a Crystal-To-Crystal Transformation. *Chem. Sci.* **2018**, *9*, 7986–7991.

(15) (a) Roubeau, O. Triazole-Based One-Dimensional Spin-Crossover Coordination Polymers. *Chem. Eur. J.* **2012**, *18*, 15230–15244. (b) Garcia, Y.; Adarsh, N. N.; Naik, A. D. Crystal Engineering of Fe$^{II}$ Spin Crossover Coordination Polymers Derived from Triazole or Tetrazole Ligands. *Chimia* **2013**, *67*, 411–418.

(16) Sciortino, N. F.; Neville, S. M. Two-Dimensional Coordination Polymers with Spin Crossover Functionality. *Aust. J. Chem.* **2014**, *67*, 1553–1562. (b) Ni, Z.-P.; Liu, J.-L.; Hoque, M. N.; Liu, W.; Li, J.-Y.; Chen, Y.-C.; Tong, M.-L. Recent Advances in Guest Effects on Spin-Crossover Behavior in Hofmann-Type Metal-Organic Frameworks.

*Coord. Chem. Rev.* **2017**, *335*, 28–43. (c) Espallargas, G. M.; Coronado, E. Magnetic Functionalities in MOFs: From the Framework to the Pore. *Chem. Soc. Rev.* **2018**, *47*, 533–557.

(17) Gaspar, A. B.; Seredyuk, M. Spin Crossover in Soft Matter. *Coord. Chem. Rev.* **2014**, *268*, 41–58.

(18) (a) Cavallini, M. Status and Perspectives in Thin Films and Patterning of Spin Crossover Compounds. *Phys. Chem. Chem. Phys.* **2012**, *14*, 11867–11876. (b) Lefter, C.; Davesne, V.; Salmon, L.; Molnár, G.; Demont, P.; Rotaru, A.; Bousseksou, A. Charge Transport and Electrical Properties of Spin Crossover Materials: Towards Nanoelectronic and Spintronic Devices. *Magnetochemistry* **2016**, *2*, 18/1–19.

(19) See *eg* (a) Harzmann, G. D.; Frisenda, R.; van der Zant, H. S. J.; Mayor, M. Single-Molecule Spin Switch Based on Voltage-Triggered Distortion of the Coordination Sphere. *Angew. Chem. Int. Ed.* **2015**, *54*, 13425–13430. (b) Aragonès, A. C.; Aravena, D.; Cerdá, J. I.; Acís-Castillo, Z.; Li, H.; Real, J. A.; Sanz, F.; Hihath, J.; Ruiz, E.; Díez-Pérez, I. Large Conductance Switching in a Single-Molecule Device through Room Temperature Spin-Dependent Transport. *Nano Lett.* **2016**, *16*, 218–226. (c) Jasper-Toennies, T.; Gruber, M.; Karan, S.; Jacob, H.; Tuczek, F.; Berndt, R. Robust and Selective Switching of an FeIII Spin-Crossover Compound on Cu$_2$N/Cu(100) with Memristance Behavior. *Nano Lett.* **2017**, *17*, 6613–6619. (d) Burzurí, E.; García-Fuente, A.; García-Suárez, V.; Kumar, K. S.; Ruben, M.; Ferrer, J.; van der Zant, H. S. J. Spin-State Dependent Conductance Switching in Single Molecule-Graphene Junctions. *Nanoscale* **2018**, *10*, 7905–7911.

(20) Hayami, S.; Holmes, S. M.; Halcrow, M. A. Spin-State Switches in Molecular Materials Chemistry. *J. Mater. Chem. C* **2015**, *3*, 7775–7778.

(21) (a) Hogue, R. W.; Singh, S.; Brooker, S. Spin Crossover in Discrete Polynuclear Iron(II) Complexes. *Chem. Soc. Rev.* **2018**, *47*, 7303–7338. (b) McConnell, A. J. Spin-State Switching in Fe(II) Helicates and Cages. *Supramol. Chem.* **2018**, *30*, 858–868.

(22) Scott, H. S.; Staniland, R. W.; Kruger, P. E. Spin Crossover in Homoleptic Fe(II) Imidazolylimine Complexes. *Coord. Chem. Rev.* **2018**, *362*, 24–43.

(23) (a) Gaspar, A. B.; Muñoz, M. C.; Real, J. A. Dinuclear Iron(II) Spin Crossover Compounds: Singular Molecular Materials for Electronics. *J. Mater. Chem.* **2006**, *16*, 2522–2533. (b) Bousseksou, A.; Molnár, G.; Real, J. A.; Tanaka, K. Spin Crossover and Photomagnetism in Dinuclear Iron(II) Compounds. *Coord. Chem. Rev.* **2007**, *251*, 1822–1833. (c) Olguín, J.; Brooker, S. Spin Crossover Active Iron(II) Complexes of Selected Pyrazole-Pyridine/Pyrazine Ligands. *Coord. Chem. Rev.* **2011**, *255*, 203–240.

(24) (a) Miller, T. F.; Holloway, L. R.; Nye, P. P.; Lyon, Y.; Beran, G. J. O.; Harman, W. H.; Julian, R. R.; Hooley, R. J. Small Structural Variations Have Large Effects on the Assembly Properties and Spin State of Room Temperature High Spin Fe(II) Iminopyridine Cages. *Inorg. Chem.* **2018**, *57*, 13386–13396. (b) Singh, S.; Hogue, R. W.; Feltham, H. L. C.; Brooker, S. Dinuclear Helicate and Tetranuclear Cage Assembly Using Appropriately Designed Ditopic Triazole-Azine Ligands. *Dalton Trans.* **2019**, *48*, doi: 10.1039/c9dt01890e

(25) Selected recent examples of SCO-active dinuclear complexes: (a) Rodríguez-Jiménez, S.; Feltham, H. L. C.; Brooker, S. Non-Porous Iron(II)-Based Sensor: Crystallographic Insights into a Cycle of Colorful Guest-Induced Topotactic Transformations. *Angew. Chem. Int. Ed.* **2016**, *55*, 15067–15071. (b) Herold, C. F.; Shylin, S. I.; Rentschler, E. Solvent-dependent SCO Behavior of Dinuclear Iron(II) Complexes with a 1,3,4-Thiadiazole Bridging Ligand. *Inorg. Chem.* **2016**, *55*, 6414–6419. (c) Milin, E.; Belaïd, S.; Patinec, V.; Triki, S.; Chastanet, G.; Marchivie, M. Dinuclear Spin-Crossover Complexes Based on Tetradentate and Bridging Cyanocarbanion Ligands. *Inorg. Chem.* **2016**, *55*, 9038–9046. (d) Hagiwara, H.; Tanaka, T.; Hora, S. Synthesis, Structure, and Spin Crossover Above Room Temperature of a Mononuclear and Related Dinuclear Double Helicate Iron(II) Complexes. *Dalton Trans.* **2016**, *45*, 17132–17140. (e) Darawsheh, M. D.; Barrios, L. A.; Roubeau, O.; Teat, S. J.; Aromí, G. Guest-Tuned Spin Crossover in Flexible Supramolecular Assemblies Templated by a Halide (Cl$^-$, Br$^-$ or I$^-$). *Chem. Commun.* **2017**, *53*, 569–572. (f) Darawsheh, M. D.; Barrios, L. A.; Roubeau, O.; Teat, S. J.; Aromí, G. Encapsulation of a Cr$^{III}$ Single-Ion Magnet within an Fe$^{II}$ Spin-Crossover Supramolecular Host. *Angew. Chem. Int. Ed.* **2018**, *57*, 13509–13513. (g) Clements, J. E.; Airey, P. R.; Ragon, F.; Shang, V.;

Kepert, C. J.; Neville, S. M. Guest-Adaptable Spin Crossover Properties in a Dinuclear Species Underpinned by Supramolecular Interactions. *Inorg. Chem.* **2018**, *57*, 14930–14938.

(26) Newton, G. N.; Nihei, M.; Oshio, H. Cyanide-Bridged Molecular Squares − the Building Units of Prussian Blue. *Eur. J. Inorg. Chem.* **2011**, *2011*, 3031–3042.

(27) Recent examples of SCO-active molecular squares: (a) Hietsoi, O.; Dunk, P. W.; Stout, H. D.; Arroyave, A.; Kovnir, K.; Irons, R. E.; Kassenova, N.; Erkasov, R.; Achim, C.; Shatruk, M. Spin Crossover in Tetranuclear Fe(II) Complexes, ⟨[(tpma)Fe(µ-CN)]₄⟩X₄ (X = ClO₄⁻, BF₄⁻). *Inorg. Chem.* **2014**, *53*, 13070–13077. (b) Mondal, A.; Li, Y.; Chamoreau, L.-M.; Seuleiman, M.; Rechignat, L.; Bousseksou, A.; Boillot, M.-L.; Lescouëzec, R. Photo- and Thermo-Induced Spin Crossover in a Cyanide-Bridged ⟨Moᵛ₂Feᴵᴵ₂⟩ Rhombus Molecule. *Chem. Commun.* **2014**, *50*, 2893–2895. (c) Zheng, C.; Xu, J.; Wang, F.; Tao, J.; Li, D. Spin Crossover and Reversible Single-Crystal to Single-Crystal Transformation Behaviour in two Cyanide-Bridged Mixed-Valence ⟨Feᴵᴵᴵ₂Feᴵᴵ₂⟩ Clusters. *Dalton Trans.* **2016**, *45*, 17254–17263.

(28) (a) Hardy, J. G. Metallosupramolecular Grid Complexes: Towards Nanostructured Materials with High-Tech Applications. *Chem. Soc. Rev.* **2013**, *42*, 7881–7899. (b) Shiga, T.; Newton, G. N.; Oshio, H. Pre-Programmed Self-Assembly of Polynuclear clusters. *Dalton Trans.* **2018**, *47*, 7384–7394.

(29) Recent examples of SCO-active grid complexes. (a) Shen, F.; Huang, W.; Wu, D.; Zheng, Z.; Huang, X.-C.; Sato, O. Redox Modulation of Spin Crossover within a Cobalt Metallogrid. *Inorg. Chem.* **2016**, *55*, 902–908. (b) Steinert, M.; Schneider, B.; Dechert, S.; Demeshko, S.; Meyer, F. Spin-State Versatility in a Series of Fe₄ [2×2] Grid Complexes: Effects of Counteranions, Lattice Solvent, and Intramolecular Cooperativity. *Inorg. Chem.* **2016**, *55*, 2363–2373. (c) Schäfer, B.; Greisch, J.-F.; Faus, I.; Bodenstein, T.; Šalitroš, I.; Fuhr, O.; Fink, K.; Schünemann, V.; Kappes, M. M.; Ruben, M. Divergent Coordination Chemistry: Parallel Synthesis of [2×2] Iron(II) Grid-Complex Tauto-Conformers. *Angew. Chem. Int. Ed.* **2016**, *55*, 10881–10885. (d) Dhers, S.; Mondal, A.; Aguilà, D.; Ramírez, J.; Vela, S.; Dechambenoit, P.; Rouzières, M.; Nitschke, J. R.; Clérac, R.; Lehn, J.-M. Spin State Chemistry: Modulation of Ligand p$K_a$ by Spin State Switching in a [2×2] Iron(II) Grid-Type Complex. *J. Am. Chem. Soc.* **2018**, *140*, 8218–8227. (e) Shiga, T.; Sato, Y.; Tachibana, M.; Sato, H.; Matsumoto, T.; Sagayama, H.; Kumai, R.; Murakami, Y.; Newton, G. N.; Oshio, H. CarboxylicAcid Functionalized Spin-Crossover Iron(II) Grids for Tunable Switching and Hybrid Electrode Fabrication. *Inorg. Chem.* **2018**, *57*, 14013–14017.

(30) Recent examples of SCO-active tetrahedral coordination cages: (a) Li, L.; Saigo, N.; Zhang, Y.; Fanna, D. J.; Shepherd, N. D.; Clegg, J. K.; Zheng, R.; Hayami, S.; Lindoy, L. F.; Aldrich-Wright, J. R.; Li, C.-G.; Reynolds, J. K.; Harman, D. G.; Li, F. A Large Spin-Crossover [Fe₄L₄]⁸⁺ Tetrahedral Cage. *J. Mater. Chem. C* **2015**, *3*, 7878–7882. (b) Han, W.-K.; Zhang, H.-X.; Wang, Y.; Liu, W.; Yan, X.; Lia, T.; Gu, Z.-G. Tetrahedral Metal−Organic Cages with Cube-Like Cavities for Selective Encapsulation of Fullerene Guests and Their Spin-Crossover Properties. *Chem. Commun.* **2018**, *54*, 12646–12649. (c) Li, L.; Craze, A. R.; Mustonen, O.; Zenno, H.; Whittaker, J. J.; Hayami, S.; Lindoy, L. F.; Marjo, C. E.; Clegg, J. K.; Aldrich-Wright, J. R.; Li, F. A mixed-spin spin-crossover thiozolylimine [Fe₄L₆]⁸⁺ cage. *Dalton Trans.* **2019**, *48*, 9935–9938.

(31) Kershaw-Cook, L. J.; Fisher, J.; Harding, L. P.; Halcrow, M. A. An Iron(II) Spin-Crossover Metallacycle from a Back-To-Back Bis-[dipyrazolylpyridine]. *Dalton Trans.* **2015**, *44*, 9417–9425.

(32) Unruh, D.; Homenya, P.; Kumar, M.; Sindelar, R.; Garcia, Y.; Renz, F. Spin State Switching of Metal Complexes by Visible Light or Hard X-Rays. *Dalton Trans.* **2016**, *45*, 14008–14018.

(33) (a) Duriska, M. B.; Neville, S. M.; Moubaraki, B.; Cashion, J. D.; Halder, G. J.; Chapman, K. W.; Balde, C.; Létard, J.-F.; Murray, K. S.; Kepert, C. J.; Batten, S. R. A Nanoscale Molecular Switch Triggered by Thermal, Light, and Guest Perturbation. *Angew. Chem. Int. Ed.* **2009**, *48*, 2549–2552. (b) Duriska, M. B.; Neville, S. M.; Moubaraki, B.; Murray, K. S.; Balde, C.; Létard, J.-F.; Kepert, C. J.; Batten, S. R. A Family of Discrete Magnetically Switchable Nanoballs. *ChemPlusChem* **2012**, *77*, 616–623.

(34) Struch, N.; Bannwarth, C.; Ronson, T. K.; Lorenz, Y.; Mienert, B.; Wagner, N.; Engeser, M.; Bill, E.; Puttreddy, R.; Rissanen, K.; Beck, J.; Grimme, S.; Nitschke, J. R.; Lützen, A. An Octanuclear Metallosupramolecular Cage Designed to Exhibit Spin-Crossover Behavior. *Angew. Chem. Int. Ed.* **2017**, *56*, 4930–4935.

(35) (a) Chorazy, S.; Podgajny, R.; Nakabayashi, K.; Stanek, J.; Rams, M.; Sieklucka, B.; Ohkoshi, S. Feᴵᴵ Spin-Crossover Phenomenon in the Pentadecanuclear ⟨Fe₉[Re(CN)₈]₆⟩ Spherical Cluster. *Angew. Chem. Int. Ed.* **2015**, *54*, 5093–5097. (b) Chorazy, S.; Stanek, J. J.; Kobylarczyk, J.; Ohkoshi, S.; Sieklucka, B.; Podgajny, R. Modulation of the Feᴵᴵ Spin Crossover Effect in the Pentadecanuclear ⟨Fe₉[M(CN)₈]₆⟩ (M = Re, W) Clusters by Facial Coordination of Tridentate Polyamine Ligands. *Dalton Trans.* **2017**, *46*, 8027–8036.

(36) Arczyński, M.; Rams, M.; Stanek, J.; Fitta, M.; Sieklucka, B.; Dunbar, K. R.; Pinkowicz, D. A Family of Octahedral Magnetic Molecules Based on [Nbᴵⱽ(CN)₈]⁴⁻. *Inorg. Chem.* **2017**, *56*, 4021–4027.

(37) (a) Shatruk, M.; Dragulescu-Andrasi, A.; Chambers, K. E.; Stoian, S. A.; Bominaar, E. L.; Achim, C.; Dunbar, K. R. Properties of Prussian Blue Materials Manifested in Molecular Complexes: Observation of Cyanide Linkage Isomerism and Spin-Crossover Behavior in Pentanuclear Cyanide Clusters. *J. Am. Chem. Soc.* **2007**, *129*, 6104–6116. (b) Funck, K. E.; Prosvirin, A. V.; Mathonière, C.; Clérac, R.; Dunbar, K. R. Light-Induced Excited Spin State Trapping and Charge Transfer in Trigonal Bipyramidal Cyanide-Bridged Complexes. *Inorg. Chem.* **2011**, *50*, 2782–2789.

(38) Yan, Z.; Liu, W.; Peng, Y.-Y.; Chen, Y.-C.; Li, Q.-W.; Ni, Z.-P.; Tong, M.-L. Spin-Crossover Phenomenon in a Pentanuclear Iron(II) Cluster Helicate. *Inorg. Chem.* **2016**, *55*, 4891–4896.

(39) Ortiz, M. I.; Soriano, M. L.; Carranza, M. P.; Jalón, F. A.; Steed, J. W.; Mereiter, K.; Rodríguez, A. M.; Quiñonero, D.; Deyà, P. M.; Manzano, B. R. New [2×2] Copper(I) Grids as Anion Receptors. Effect of Ligand Functionalization on the Ability to Host Counteranions by Hydrogen Bonds. *Inorg. Chem.* **2010**, *49*, 8828–8847.

(40) Hübsch, W.; Pfleiderer, W. Pteridines. Part XLII. Synthesis and Properties of 6,7,8-Trimethyl-4-thiolumazine. *Helv. Chim. Acta* **1989**, *72*, 738–743.

(41) Sheldrick, G. M. Crystal Structure Refinement with *SHELXL*. *Acta Cryst. Sect. C.: Struct. Chem.* **2015**, *71*, 3–8.

(42) Barbour, L. J. *X-Seed* − A Software Tool for Supramolecular Crystallography. *J. Supramol. Chem.* **2001**, *1*, 189–191.

(43) Dolomanov, O. V.; Bourhis, L. J.; Gildea, R. J.; Howard, J. A. K.; Puschmann, H. *OLEX2*: a Complete Structure Solution, Refinement and Analysis Program. *J. Appl. Cryst.* **2009**, *42*, 339–341.

(44) Brown, I. D. https://www.iucr.org/resources/data/datasets/bond-valence-parameters

(45) Yvon, K.; Jeitschko, W.; Parthé, E. *LAZY PULVERIX,* a computer program, for calculating X-ray and neutron diffraction powder patterns. *J. Appl. Cryst.* **1977**, *10*, 73–74.

(46) O'Connor, C. J. Magnetochemistry − Advances in Theory and Experimentation. *Prog. Inorg. Chem.* **1982**, *29*, 203–283.

(47) (a) Evans, D. F. The Determination of the Paramagnetic Susceptibility of Substances in Solution by Nuclear Magnetic Resonance. *J. Chem. Soc.* **1959**, 2003–2005. (b) Schubert, E. M. Utilizing the Evans Method with a Superconducting NMR Spectrometer in the Undergraduate Laboratory. *J. Chem. Educ.* **1992**, *69*, 62.

(48) García, B.; Ortega, J. C. Excess Viscosity $\eta^E$, Excess Volume $V^E$, and Excess Free Energy of Activation $\Delta G^{*E}$ at 283, 293, 303, 313, and 323 K for Mixtures of Acetonitrile and Alkyl Benzoates. *J. Chem. Eng. Data* **1988**, *33*, 200–204.

(49) Létard, J.-F.; Guionneau, P.; Rabardel, L.; Howard, J. A. K.; Goeta, A.; Chasseau, D.; Kahn, O. Structural, Magnetic, and Photomagnetic Studies of a Mononuclear Iron(II) Derivative Exhibiting an Exceptionally Abrupt Spin Transition. Light-Induced Thermal Hysteresis Phenomenon. *Inorg. Chem.* **1998**, *37*, 4432–4441.

(50) Gunnlaugsson, H. P. Spreadsheet Based Analysis of Mössbauer Spectra. *Hyperfine Interact.* **2016**, *237*, 79/1–6.

(51) O'Keeffe, M. The Prediction and Interpretation of Bond Lengths in Crystals. *Struct. Bonding (Berlin)* **1989**, *71*, 161–190.

(52) The internal volume of the [Fe₈(µ-L¹)₁₂]⁴⁺ cage in **1**·6MeCN was calculated to be 89.6 Å³ at 250 K and 92.5 Å³ at 100 K, using a 0.2 Å probe sphere. Corresponding values for [Fe₈(µ-L²)₁₂]⁴⁺ in **2**·$x$MeCN·$y$Et₂O are 90.3 Å³ at 250 K and 88.2 Å³ at 125 K. The slightly larger volume for **1**·6MeCN at low temperature should be interpret-

(53) Cao, M.-L.; Hao, H.-G.; Zhang, W.-X; Ye, B.-H. Assembly of a Cubic Nanocage $Co_8L_{12}$ and a Hydrogen-Bonded 3D NbO Net Based on the $[(HCO_3)_2]^{2-}$ Synthon and Water. *Inorg. Chem.* **2008**, *47*, 8126−8133.

(54) Gordon, A. J.; Ford, R. A. *The Chemists Companion − a Handbook of Practical Data, Techniques and References*, John Wiley and Sons, Chichester, 1972.

(55) Guionneau, P.; Marchivie, M.; Bravic, G.; Létard, J.-F.; Chasseau, D. Structural Aspects of Spin Crossover. Example of the $[Fe^{II}L_n(NCS)_2]$ Complexes. *Top. Curr. Chem.* **2004**, *234*, 97−128.

(56) $\Sigma$ is the sum of the deviations of each *cis*-N–Fe–N bond angle from 90°. A perfect octahedral complex gives $\Sigma$ = 0, with larger values indicating more distorted coordination geometries.[55]

(57) Boča, R. Zero-Field Splitting in Metal Complexes. *Coord. Chem. Rev.* **2004**, *248*, 757−815.

(58) Antiferromagnetic exchange between the high-spin iron(II) ions should also contribute to the low-temperature magnetic behavior of **1** and **2**.[59,68] However, precedent suggests this will be 5-10x smaller than the zero field splitting, with $J \approx -1$ cm$^{-1}$.[69]

(59) Létard, J.-F.; Real, J. A.; Moliner, N.; Gaspar, A. B.; Capes, L.; Cador, O.; Kahn, O. Light Induced Excited Pair Spin State in an Iron(II) Binuclear Spin-Crossover Compound. *J. Am. Chem. Soc.* **1999**, *121,* 10630−10631.

(60) Knudsen, J. E. Mössbauer Spectroscopic Studies of the Magnetic Hyperfine Interaction in the Ferric Hexaquo Complex in Frozen Aqueous Solution. *J. Phys. Chem. Solids* **1977**, *38*, 883−896.

(61) Schünemann, V.; Winkler, H. Structure and Dynamics of Biomolecules Studied by Mössbauer Spectroscopy. *Rep. Prog. Phys.* **2000**, *63*, 263−353.

(62) Hauser, A. Light-Induced Spin Crossover and the High-Spin→Low-Spin Relaxation. *Top. Curr. Chem.* **2004**, *234*, 155−198.

(63) (a) Létard, J.-F. Photomagnetism of Iron(II) Spin Crossover Complexes − the *T*(LIESST) Approach. *J. Mater. Chem.* **2006**, *16*, 2550−2559. (b) Chastanet, G.; Desplanches, C.; Baldé, C.; Rosa, P.; Marchivie, M.; Guionneau, P. A Critical Review of the *T*(LIESST) Temperature in Spin Crossover Materials − What it is and What it is Not. *Chem. Sq.* **2018**, *2*, 2/1−19.

(64) The maximum $\chi_M T$ value on warming the irradiated sample of **1**, before the onset of LIESST relaxation, is 25.1 cm$^3$mol$^{-1}$K compared to a 'dark' measurement of 22.7 cm$^3$mol$^{-1}$K at the same temperature, a difference of 2.4 cm$^3$mol$^{-1}$K. The corresponding $\chi_M T$ maximum for **2** after irradiation is 25.8 cm$^3$mol$^{-1}$K at 50 K, which is 4.6 cm$^3$mol$^{-1}$K higher than the 'dark' measurement of 21.2 cm$^3$mol$^{-1}$K. Assuming two low-spin Fe(II) sites per cubane undergo LIESST excitation, that corresponds to *ca* 35 and 65 % photoconversion efficiency in **1** and **2** respectively. Different exchange coupling and zero-field splitting contributions to $\chi_M T$ in the dark and irradiated materials are potential sources of error in these estimates however.[59,68]

(65) Létard, J.-F.; Capes, L.; Chastanet, G.; Moliner, N.; Létard, S.; Real, J. A.; Kahn, O. Critical Temperature of the LIESST Effect in Iron(II) Spin Crossover Compounds. *Chem. Phys. Lett.* **1999**, *313*, 115−120.

(66) Wenger, O. S. Is Iron the New Ruthenium? *Chem. Eur. J.* **2019**, *25*, 6043−6052.

(67) Esteban-Gómez, D.; Fabbrizzi, L.; Licchelli, M. Why, on Interaction of Urea-Based Receptors with Fluoride, Beautiful Colors Develop. *J. Org. Chem.* **2005**, *70*, 5717−5720.

(68) Sun, H.-Y.; Meng, Y.-S.; Liu, T. Photo-Switched Magnetic Coupling in Spin-Crossover Complexes. *Chem. Commun.* **2019**, *55*, 8359−8373.

(69) (a) Oshio, H.; Ichida, H. Control of Intramolecular Magnetic Interaction by the Spin Polarization of $d_\pi$ Spin to $p_\pi$ Orbital of an Organic Bridging Ligand. *J. Phys. Chem.* **1995**, *99*, 3294−3302. (b) Gobeze, W. A.; Milway, V. A.; Olguín, J.; Jameson, G. N. L.; Brooker, S. Nine Diiron(II) Complexes of Three Bis-tetradentate Pyrimidine Based Ligands with NCE (E = S, Se, BH$_3$) Coligands. *Inorg. Chem.* **2012**, *51*, 9056−9065.